Band Structure and Fermi-Surface Properties of Ordered β-Brass

H. L. Skriver and N. E. Christensen

Physics Laboratory I, The Technical University of Denmark, DK-2800 Lyngby, Denmark

(Received 21 May 1973)

The band structure of ordered β-brass (β′-CuZn) has been calculated throughout the Brillouin zone by the augmented-plane-wave method. The present band model differs from previous calculations with respect to the position and width of the Cu $3d$ band. The derived dielectric function $\epsilon_2(\omega)$ and the photoemission spectra agree well with experiments. We find that the main absorption edge as observed in the ϵ_2 trace has contributions from conduction-band transitions as well as transitions from the Cu d states. The comparison to photoemission results indicates that the calculated Cu d bands are too narrow, but that their position relative to the Fermi level is correct. The derived Fermi-surface model allows a detailed interpretation of the de Haas–van Alphen (dHvA) data. The present model has no open orbit along $<100>$ for $\vec{B}\parallel<110>$. This agrees with dHvA as well as magnetoresistance measurements. Four new extremal cross sections have been found and related to previously unexplained dHvA frequencies. In general, the Fermi-surface dimensions agree extremely well with dHvA measurements, and the ratios between the experimental and the calculated cyclotron masses vary between 1.18 and 1.43.

I. INTRODUCTION

Ordered β-brass (β'-CuZn) crystallizes in the simple-cubic CsCl structure and is one of the simplest types of alloys. It has approximately 1.5 valence electrons per atom, and Hume-Rothery[1] recognized this ratio as characteristic for alloy phases, such as the β' phase, that only exist in a narrow range of composition. These so-called electron compounds include among others β'-CuZn, β'-AgZn, β'-PdIn, and β'-NiAl.

The electronic energy band structure of β'-CuZn has been subjected to several experimental studies including optical excitations from far below the Fermi level (E_F) as well as Fermi surface experiments. Static reflectance measurements[2-4] show a strong absorption edge at the photon energy 2.5 eV, and this fundamental edge has been attributed to interband transitions between conduction bands with the initial states at the Fermi level. From the photoemission measurements[5] it was, however, concluded that the edge was rather due to transitions from the Cu d band. Also, "bands of strong d character" were found[5] to start at about 2.5 eV below E_F in contrast to the 3.7 eV suggested in the interpretation[3] of the reflectance measurements.

Experimental information on the electronic properties of β'-CuZn at the Fermi level has been deduced from measurements of specific heat,[6] Hall effect,[7] magnetoresistance,[8] and in particular from the extensive de Haas–van Alphen (dHvA) experiments.[9-12] The Fermi surface is found to be multiply connected with open orbits[8] when $\vec{B}$ lies in {100} and {110} planes.

Several band models based on "first-principles" calculations have been published.[13-18] They all agree as to the qualitative features of the s, p, and d bands but disagree in the position of the Cu d

band (Table I). The differences between the d band data listed in Table I reflect the fact that the d band parameters, width and position, respond sensitively to changes in the crystal potential as is also seen in the noble and transition metals. According to the particular position of the Cu d band the absorption edge has been attributed to either transitions between conduction states[13-15,18] or to transitions from the Cu d band.[16,17]

The Fermi-surface models[13,15-18] derived from previous calculations agree qualitatively showing the existence of a hole sheet in the first zone, multiply connected sheets in the second zone, and no overlap into the third and fourth zones. However, all the models suggest the existence of open orbits along the $\langle 100 \rangle$ direction in contradiction to the high-field magnetoresistance experiments.[8] Although the latest calculation by Arlinghaus[18] also exhibits this discrepancy the derived extremal cross sections for fields along symmetry directions are in fair agreement with the dHvA measurements. It still leaves, however, several of the experimental dHvA frequencies unexplained.

Comparing the early dHvA results[9] to a pseudopotential calculation of the angular variation of extremal Fermi-surface cross sections, Taylor[19] suggested a connection between dHvA branches and orbits on the Fermi surface. The most recent experiments,[12] however, give new dHvA branches, and few of the assignments made by Taylor are still valid. A new set of assignments has appeared in a perliminary account of the present Fermi-surface calculations.[20]

In the present paper we present an augmented-plane-wave (APW) calculation performed very much along the lines of previous work.[17,18] The energy-band calculation which covers the entire Brillouin zone is applied for evaluation of density-of-states

TABLE I. First-principles calculations of the electronic structure of β' -CuZn and the corresponding position and width of the Cu d band. The position is defined by referring to the position of the top of the d band and the width is taken as the energy separation $X_2' - X_1$.

Reference	Method[a]	Location of Cu d band below E_F (eV)	Width of Cu d band (eV)
Johnson and Amar (Refs. 13 and 14)	KKR	10.2, 5.4	
Amar, Johnson, and Wang (Ref. 15)	KKR	4.8	~2.0
Arlinghaus (Refs. 16 and 17)	APW	2.6[b]	2.7
Arlinghaus (Ref. 18)	APW	3.3[c]	~1.9
Present calc.	APW	3.1[b], 2.9[d]	2.4

[a]Korringa–Kohn–Rostoker (KKR) or augmented plane wave (APW).

[b]$\Delta_2' \to E_F$.

[c]$T_1' \to E_F$.

[d]$R_{12}' \to E_F$.

functions, optical absorption spectra, and photo-emission energy distribution curves (EDC). The optical functions are calculated in a crude model assuming constant matrix elements. The EDC's include simplified escape functions and are calculated in the fully direct model as well as the non-direct model. So far only bulk contributions to the photoemission spectra are included, but the effect of surface emission will be commented on briefly. The calculation further includes a rather detailed examination of the Fermi surface. Thus, the angular variations of the dHvA frequencies are derived for rotation in the {100} and {110} planes. The cyclotron masses and their angular variations are also calculated.

The paper then contains three main parts: the numerical band calculations, the optical spectra, and the Fermi-surface properties. Section II contains a brief description of the crystal potential calculation and a comparison with other models. In Sec. III the calculated energy bands are presented and density-of-states functions are derived. Section III also contains a comparison of the calculated optical spectra with the static reflectance
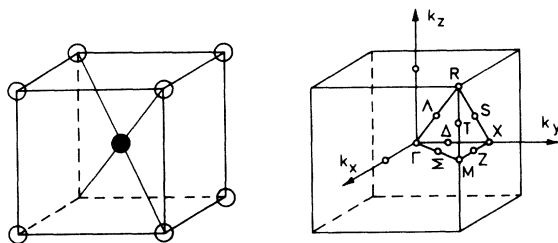

FIG. 1. Unit cell and Brillouin zone for the simple cubic CsCl structure. BSW (Ref. 26) notation is used.
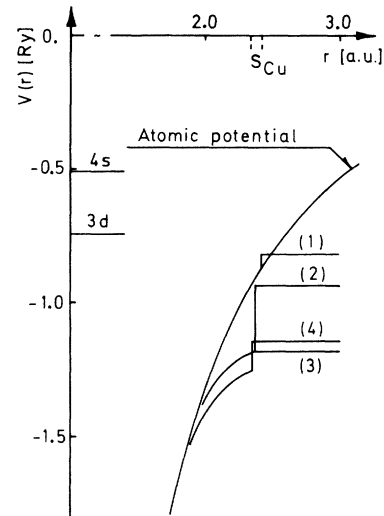

FIG. 2. Some muffin-tin potentials for the Cu site in β' -CuZn. The atomic $3d$ and $4s$ levels are indicated. (1) Potential labeled b in Ref. 15; (2) Arlinghaus (Ref. 18); (3) Arlinghaus (Refs. 16 and 17); (4) present potential.

and the photoemission experiments. In Sec. IV we present the Fermi-surface model and compare with other theoretical models. The model is further compared to de Haas–van Alphen measurements and the apparent mass enhancement is obtained.

II. CRYSTAL POTENTIAL

The simple APW method requires a crystal potential of the muffin-tin type, i.e., a potential that is spherically symmetric inside spheres and constant in the interstitial region. Since, in the simple-cubic (CsCl) structure of the fully ordered β' phase, this interstitial region occupies only 32% of the cell volume, assuming spheres of equal size, the muffin-tin approximation is a reasonable one

TABLE II. Crystal potential data from various first-principles calculations on β' -CuZn. Listed are the lattice constant a, the muffin-tin radii S_ν, the discontinuities D_ν at the muffin-tin spheres, and the constant potential E_{MTZ} between the spheres.

	Amar, Johnson and Wang (Ref. 15)	Arlinghaus (Ref. 17)	Arlinghaus (Ref. 18)	Present calc.
a(Å)	2.944[a]	2.9539[b]	2.9539[b]	2.944[a]
S_{Zn}(a. u.)	2.41	2.473	2.473	2.460
S_{Cu}(a. u.)	2.41	2.361	2.361	2.340
D_{Zn}(Ry)	~0.16[c]	0	0.2396	0.1125
D_{Cu}(Ry)	~0.06[c]	0	0.2435	0.1166
E_{MTZ}(Ry)	~-0.82[c]	-1.1797	~-0.936	-1.1385

[a]At 4.2 °K from Ref. 9.

[b]At 29.8 °K.

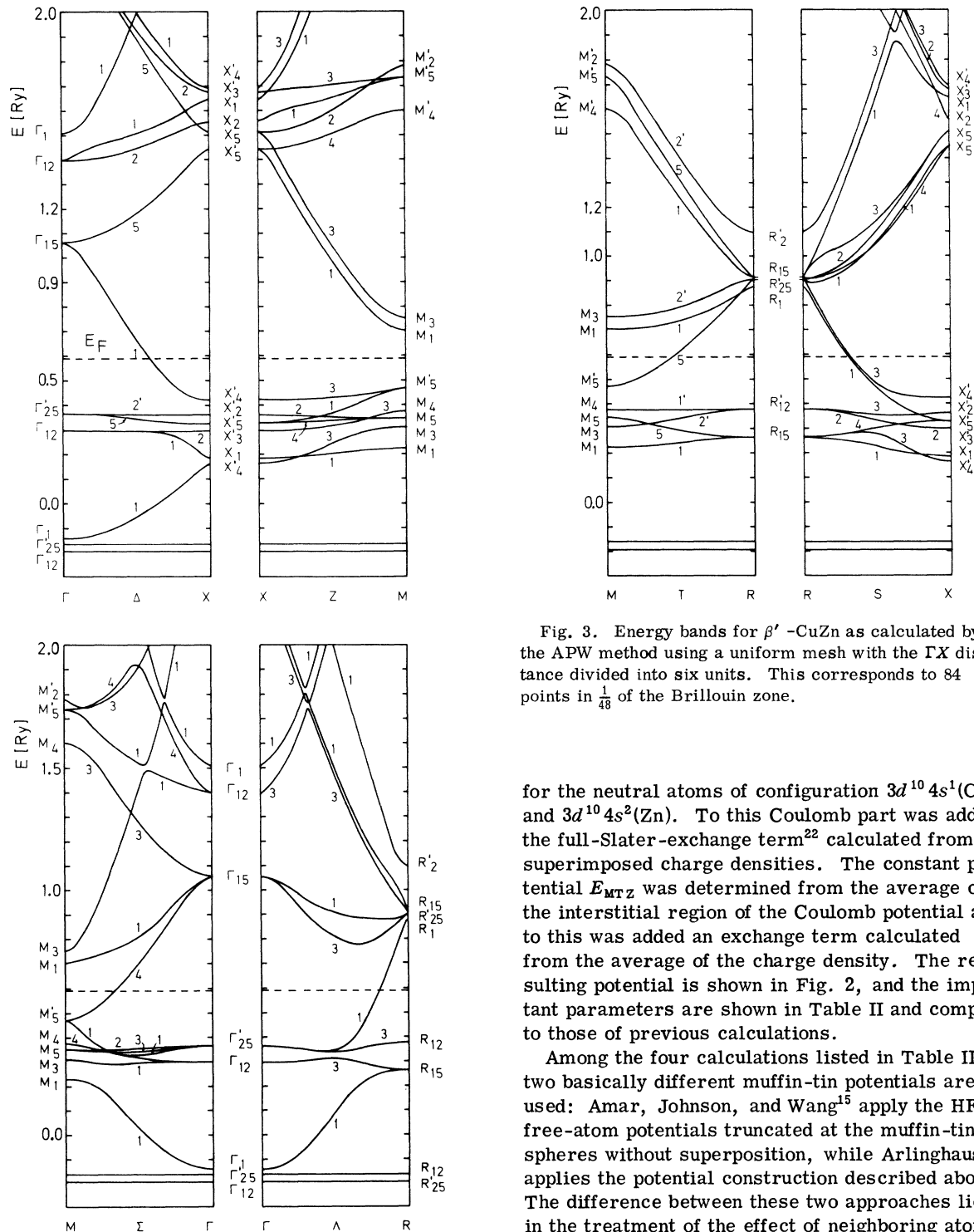[c]Values for the potential labeled b in Ref. 15.

Fig. 3. Energy bands for β' -CuZn as calculated by the APW method using a uniform mesh with the ΓX distance divided into six units. This corresponds to 84 points in $\frac{1}{48}$ of the Brillouin zone.

for β'-CuZn. The spherically symmetric part of the crystal potential has been constructed by a superposition in the CsCl structure (Fig. 1) of atomic Coulomb potentials derived from the Hartree-Fock-Slater[21] (HFS) atomic charge densities

for the neutral atoms of configuration $3d^{10} 4s^1$(Cu) and $3d^{10} 4s^2$(Zn). To this Coulomb part was added the full-Slater-exchange term[22] calculated from superimposed charge densities. The constant potential E_{MTZ} was determined from the average over the interstitial region of the Coulomb potential and to this was added an exchange term calculated from the average of the charge density. The resulting potential is shown in Fig. 2, and the important parameters are shown in Table II and compared to those of previous calculations.

Among the four calculations listed in Table II, two basically different muffin-tin potentials are used: Amar, Johnson, and Wang[15] apply the HFS free-atom potentials truncated at the muffin-tin spheres without superposition, while Arlinghaus[16-18] applies the potential construction described above. The difference between these two approaches lies in the treatment of the effect of neighboring atoms. Amar et al. ignore this effect in the spherically symmetric part, and overlap is included only in the constant potential E_{MTZ} which in this case is treated as an adjustable parameter. This is in contrast to other methods applying the average over the interstitial region calculated either directly as in the present work or by the Ewald method as done by

TABLE III. APW eigenvalues at a mesh uniformly distributed in $\frac{1}{48}$ zone. Energies are in rydberg relative to the muffin-tin zero E_{MTZ}. $E_F = 0.590$ Ry.

$\vec{k}$ ($\pi/6a$)	Band 1	Band 2	Band 3	Band 4	Band 5	Band 6	Band 7	Band 8	Band 9	Band 10	Band 11	Band 12	Band 13
000	−0.1401	0.2970	0.2970	0.3631	0.3631	0.3631	1.0653	1.0653	1.0653	1.3952	1.3952	1.5079	
100	−0.1309	0.2966	0.2966	0.3627	0.3627	0.3627	0.9775	1.0786	1.0786	1.4006	1.4466	1.5659	>2.0
110	−0.1215	0.2973	0.2973	0.3562	0.3568	0.3617	0.9801	0.9987	1.0925	1.4261	1.5084	1.5961	
111	−0.1122	0.2979	0.2979	0.3535	0.3574	0.3588	0.9919	0.9919	1.0195	1.5150	1.5150	1.6185	
200	−0.1031	0.2966	0.2981	0.3521	0.3521	0.3619	0.8215	1.1181	1.1181	1.4162	1.4784	1.7515	1.9000
210	−0.0936	0.2970	0.2989	0.3490	0.3511	0.3604	0.8313	1.0253	1.1301	1.4450	1.5612	1.7604	1.8923
211	−0.0843	0.2982	0.2995	0.3475	0.3503	0.3582	0.8413	1.0267	1.0457	1.5346	1.5854	1.7690	1.8120
220	−0.0657	0.2978	0.3023	0.3420	0.3484	0.3580	0.8378	0.8917	1.1659	1.4648	1.7288	1.7302	1.8183
221	−0.0566	0.2995	0.3028	0.3421	0.3474	0.3549	0.8495	0.8989	1.0695	1.5754	1.7353	1.7376	1.8183
222	−0.0297	0.3046	0.3046	0.3411	0.3462	0.3462	0.8833	0.8833	0.9501	1.7400	1.7400	1.7623	1.7623
300	−0.0567	0.2967	0.2967	0.3431	0.3431	0.3613	0.6675	1.1792	1.1792	1.4428	1.5060	1.9035	1.9035
310	−0.0474	0.2972	0.2997	0.3405	0.3433	0.3597	0.6769	1.0799	1.1903	1.4722	1.5957	1.7434	1.9098
311	−0.0383	0.2988	0.3004	0.3409	0.3412	0.3579	0.6865	1.0817	1.0984	1.5675	1.6210	1.7386	1.7642
320	−0.0200	0.2976	0.3052	0.3344	0.3433	0.3566	0.7020	0.9222	1.2235	1.4901	1.5717	1.7956	1.9243
321	−0.0113	0.2998	0.3056	0.3353	0.3419	0.3539	0.7121	0.9355	1.1207	1.5720	1.6140	1.7686	1.8446
322	0.0144	0.3059	0.3066	0.3365	0.3396	0.3479	0.7401	0.9370	0.9797	1.5868	1.6092	1.7887	1.7978
330	0.0244	0.2966	0.3132	0.3284	0.3425	0.3537	0.7051	0.8088	1.2771	1.4071	1.5212	1.9193	1.9193
331	0.0324	0.2991	0.3132	0.3295	0.3422	0.3506	0.7175	0.8148	1.1687	1.4155	1.6421	1.7917	1.8077
332	0.0561	0.3057	0.3129	0.3320	0.3430	0.3437	0.7534	0.8307	1.0073	1.4382	1.6248	1.6452	1.8461
333	0.0943	0.3113	0.3113	0.3361	0.3370	0.3494	0.8100	0.8100	0.9046	1.4701	1.4701	1.4950	1.9830
400	0.0072	0.2893	0.2969	0.3349	0.3349	0.3608	0.5358	1.2597	1.2597	1.4803	1.5440	1.7503	1.7503
410	0.0161	0.2896	0.2983	0.3344	0.3359	0.3592	0.5436	1.1521	1.2700	1.5095	1.6010	1.6416	1.7574
411	0.0248	0.2907	0.2997	0.3326	0.3380	0.3577	0.5519	1.1538	1.1691	1.5878	1.6163	1.6257	1.6668
420	0.0423	0.2898	0.3045	0.3337	0.3378	0.3561	0.5660	0.9888	1.3002	1.4229	1.5329	1.7775	1.8398
421	0.0503	0.2922	0.3052	0.3305	0.3413	0.3541	0.5753	0.9969	1.1893	1.4313	1.6280	1.6563	1.8513
422	0.0740	0.2977	0.3078	0.3271	0.3470	0.3496	0.6015	1.0074	1.0391	1.4451	1.4642	1.8226	1.8501
430	0.0837	0.2896	0.3156	0.3332	0.3402	0.3525	0.5960	0.8407	1.2629	1.3491	1.5582	1.8018	1.8452
431	0.0908	0.2924	0.3158	0.3293	0.3450	0.3502	0.6072	0.8479	1.2337	1.2709	1.6599	1.6852	1.8312
432	0.1113	0.2996	0.3136	0.3269	0.3459	0.3539	0.6385	0.8690	1.0680	1.2938	1.4923	1.6822	1.8764
433	0.1432	0.3050	0.3065	0.3328	0.3441	0.3673	0.6840	0.8822	0.9377	1.3245	1.3413	1.5298	1.8935
440	0.1363	0.2887	0.3312	0.3344	0.3419	0.3498	0.5936	0.7570	1.1181	1.4143	1.5949	1.7945	1.8180
441	0.1418	0.2914	0.3270	0.3295	0.3495	0.3509	0.6079	0.7619	1.1258	1.2944	1.6888	1.7025	1.7386
442	0.1577	0.2969	0.3165	0.3281	0.3498	0.3678	0.6479	0.7765	1.1260	1.1497	1.5385	1.5483	1.8551
443	0.1813	0.2976	0.3042	0.3373	0.3508	0.3925	0.7085	0.7991	0.9722	1.1883	1.3816	1.3938	1.7791
444	0.2080	0.2928	0.2928	0.3512	0.3512	0.4317	0.7860	0.7860	0.8836	1.2365	1.2365	1.2599	1.6510
500	0.0858	0.2513	0.2971	0.3292	0.3292	0.3604	0.4491	1.3570	1.3570	1.5259	1.5964	1.6100	1.6100
510	0.0941	0.2533	0.2986	0.3307	0.3320	0.3588	0.4528	1.2382	1.3659	1.4686	1.5636	1.6186	1.6986
511	0.1021	0.2557	0.3005	0.3265	0.3398	0.3576	0.4572	1.2389	1.2548	1.4705	1.4854	1.6781	1.7239
520	0.1177	0.2594	0.3044	0.3337	0.3398	0.3559	0.4648	1.0707	1.2960	1.3924	1.5819	1.6426	1.7523
521	0.1247	0.2625	0.3061	0.3254	0.3505	0.3544	0.4717	1.0785	1.2719	1.3042	1.5013	1.7132	1.8874
522	0.1443	0.2712	0.3102	0.3196	0.3510	0.3651	0.4920	1.0915	1.1151	1.3190	1.3360	1.8523	1.9154

TABLE III. (Continued)

$\dfrac{\vec{k}}{\pi/6a}$	Band 1	Band 2	Band 3	Band 4	Band 5	Band 6	Band 7	Band 8	Band 9	Band 10	Band 11	Band 12	Band 13
530	0.1523	0.2703	0.3147	0.3378	0.3503	0.3524	0.4861	0.9152	1.1351	1.4350	1.6077	1.6801	1.7621
531	0.1576	0.2737	0.3158	0.3273	0.3509	0.3624	0.4957	0.9234	1.1429	1.3128	1.5380	1.7321	1.8459
532	0.1725	0.2826	0.3118	0.3231	0.3486	0.3808	0.5227	0.9458	1.1443	1.1664	1.3668	1.7353	1.8803
533	0.1936	0.2910	0.3022	0.3317	0.3491	0.4046	0.5641	0.9695	1.0020	1.1954	1.2172	1.5933	1.7958
540	0.1884	0.2859	0.3329	0.3418	0.3491	0.3616	0.5114	0.7897	0.9916	1.4905	1.6421	1.7225	1.7664
541	0.1918	0.2886	0.3288	0.3304	0.3514	0.3762	0.5251	0.7958	0.9991	1.3683	1.5863	1.7239	1.7851
542	0.2015	0.2927	0.3132	0.3278	0.3550	0.4034	0.5618	0.8145	1.0218	1.2011	1.4204	1.6047	1.7910
543	0.2156	0.2909	0.2980	0.3384	0.3579	0.4407	0.6147	0.8473	1.0372	1.0674	1.2627	1.4552	1.6677
544	0.2309	0.2857	0.2867	0.3523	0.3618	0.4919	0.6785	0.8778	0.9216	1.1047	1.1324	1.3148	1.5328
550	0.2126	0.2995	0.3444	0.3471	0.3569	0.3872	0.5091	0.7285	0.8704	1.5500	1.6829	1.7444	1.7556
551	0.2151	0.3020	0.3329	0.3338	0.3625	0.4074	0.5270	0.7326	0.8773	1.4356	1.6339	1.6474	1.7707
552	0.2221	0.3007	0.3136	0.3273	0.3663	0.4474	0.5740	0.7455	0.8983	1.2720	1.4857	1.4873	1.6911
553	0.2324	0.2891	0.2951	0.3406	0.3685	0.4981	0.6408	0.7689	0.9339	1.1166	1.3290	1.3356	1.5500
554	0.2437	0.2788	0.2813	0.3572	0.3700	0.5602	0.7232	0.8041	0.9584	1.0045	1.1832	1.1978	1.4116
555	0.2533	0.2719	0.2732	0.3699	0.3712	0.6356	0.8201	0.8201	0.8809	1.0500	1.0500	1.0934	1.2893
600	0.1622	0.1859	0.2972	0.3274	0.3274	0.3603	0.4231	1.4427	1.4427	1.5107	1.5107	1.5561	1.6492
610	0.1721	0.1880	0.2988	0.3288	0.3313	0.3588	0.4236	1.3117	1.3825	1.4494	1.5208	1.6007	1.6870
611	0.1816	0.1901	0.3009	0.3242	0.3415	0.3577	0.4249	1.3082	1.3316	1.3886	1.3934	1.7231	1.7758
620	0.1941	0.2004	0.3046	0.3322	0.3445	0.3559	0.4260	1.1424	1.2090	1.4700	1.5509	1.6234	1.6944
621	0.1963	0.2086	0.3068	0.3232	0.3546	0.3593	0.4284	1.1497	1.2173	1.3426	1.4165	1.7579	1.8360
622	0.2026	0.2316	0.3130	0.3151	0.3517	0.3851	0.4360	1.1629	1.1828	1.2338	1.2507	1.8648	1.9539
630	0.2032	0.2421	0.3146	0.3368	0.3525	0.3683	0.4305	0.9864	1.0476	1.5026	1.5996	1.6515	1.7065
631	0.2054	0.2479	0.3163	0.3256	0.3514	0.3857	0.4353	0.9937	1.0556	1.3782	1.4578	1.7627	1.8376
632	0.2117	0.2628	0.3110	0.3219	0.3497	0.4189	0.4502	1.0159	1.0793	1.2109	1.4843	1.7886	1.8619
633	0.2211	0.2787	0.3006	0.3315	0.3508	0.4609	0.4773	1.0500	1.0582	1.1012	1.1411	1.6418	1.7349
640	0.2128	0.2836	0.3329	0.3414	0.3492	0.4035	0.4390	0.8510	0.9064	1.5435	1.6639	1.6859	1.7186
641	0.2151	0.2864	0.3295	0.3295	0.3523	0.4225	0.4487	0.8577	0.9137	1.4276	1.5131	1.7361	1.8142
642	0.2215	0.2902	0.3103	0.3279	0.3566	0.4622	0.4763	0.8785	0.9359	1.2639	1.3412	1.6494	1.7408
643	0.2310	0.2874	0.2945	0.3387	0.3604	0.5124	0.5196	0.9148	0.9724	1.1084	1.1820	1.5086	1.5989
644	0.2413	0.2819	0.2837	0.3526	0.3653	0.5719	0.5782	0.9650	0.9714	0.9978	1.0659	1.3714	1.4594
650	0.2202	0.3040	0.3448	0.3469	0.3624	0.4459	0.4558	0.7462	0.7973	1.5830	1.7191	1.7299	1.7365
651	0.2225	0.3072	0.3327	0.3344	0.3671	0.4664	0.4735	0.7514	0.8031	1.4866	1.5788	1.6744	1.7553
652	0.2290	0.3059	0.3111	0.3269	0.3705	0.5133	0.5173	0.7680	0.8211	1.3310	1.4116	1.5381	1.6269
653	0.2386	0.2904	0.2919	0.3412	0.3723	0.5729	0.5771	0.7987	0.8528	1.1782	1.2532	1.3890	1.4771
654	0.2490	0.2773	0.2781	0.3581	0.3737	0.6416	0.6495	0.8472	0.8983	1.0390	1.1107	1.2485	1.3363
655	0.2574	0.2693	0.2702	0.3704	0.3754	0.7194	0.7324	0.9070	0.9259	0.9305	1.0133	1.1225	1.2158
660	0.2231	0.3088	0.3462	0.3462	0.3759	0.4701	0.4701	0.7009	0.7512	1.6011	1.7346	1.7346	1.7812
661	0.2254	0.3131	0.3340	0.3340	0.3760	0.4920	0.4920	0.7044	0.7554	1.5277	1.6288	1.6288	1.7038
662	0.2304	0.3115	0.3115	0.3251	0.3764	0.5453	0.5453	0.7156	0.7688	1.3858	1.4668	1.4668	1.5555
663	0.2416	0.2911	0.2911	0.3419	0.3770	0.6167	0.6167	0.7364	0.7931	1.2388	1.3112	1.3112	1.4019
664	0.2521	0.2765	0.2765	0.3594	0.3777	0.7011	0.7011	0.7703	0.8302	1.1045	1.1652	1.1652	1.2624
665	0.2603	0.2669	0.2669	0.3726	0.3785	0.7990	0.7990	0.8207	0.8772	0.9896	1.0309	1.0309	1.1499
666	0.2636	0.2636	0.2636	0.3776	0.3776	0.8772	0.9068	0.9068	0.9068	0.9112	0.9112	0.9112	1.0978

Arlinghaus.[18]

The comparison in Fig. 2 shows that the present result agrees well with the potentials used by Arlinghaus[16-18] inside the spheres taking account of the different lattice constants used (Table II), whereas it differs considerably from the potential used by Amar, Johnson, and Wang.[15] In the interstitial region the present potential differs markedly also from the latest potential calculated by Arlinghaus.[18] This is exemplified by the difference of a factor 2 in the discontinuities D_ν at the muffin-tin spheres (Table II). In view of the methods used to construct the potentials, the discontinuities obtained by Arlinghaus should be very nearly equal those of the present work. Considering the difference mentioned, we might add that the present results agree well with the cases of copper,[23] silver,[24] and gold[25] where, by solving an Ewald problem, we find a D_ν of the order of 100 mRy and an E_{MTZ} around -1.15 Ry.

As a result of this comparison of the potentials we expect the band structure derived from the present potential to be very similar to the results obtained by Arlinghaus[16-18] except for the position and width of the d bands. We also expect the two Fermi-surface models to be very similar.

III. ENERGY BANDS

The band structure for β'-brass as calculated by the APW method over a wide energy range is presented in Fig. 3 for $\vec{k}$ along all the symmetry lines of the Brillouin zone (see Fig. 1). A list of the eigenvalues obtained at 84 k points uniformly distributed in $\frac{1}{48}$ zone is provided in Table III. Convergence tests showed that even the d bands have converged to within 4 mRy. We have used the Bouchaert-Smoluchowski-Wigner (BSW)[26] symmetry symbols and have taken the Zn site as the origin for the wave functions. Therefore the Zn band appears in the present calculation at R as the d-like states R'_{25} and R_{12}, while the same band in previous calculations[16-18] appears as p-like R_{15} and R'_{12}. The reverse is true for the Cu d band at R.

Among the transition and noble metals the d bands play an important role. In copper a $3d$ band of width 250 mRy is positioned below the Fermi level in the s-p band,[27] and in going to zinc the $3d$ band seems to fall below the bottom of the s band and become very narrow.[28] In ordered β'-brass it appears from Fig. 3 that the Cu and Zn $3d$ bands are narrow and well separated while the broad $4s$, $4p$, $4d$, and $4f$ bands of both Cu and Zn form a common conduction band. The Cu $3d$ band is situated in the conduction band just below the Fermi level and the Zn $3d$ band lies below the bottom of the conduction band. The general appearance of the present energy bands agrees well with other calculations,[15-18] and the level of agreement can be judged from Table IV where the positions and the widths of the various bands are listed. The Cu result is shown for comparison.

In β'-CuZn the Cu-Cu distance is larger and the coordination number is smaller than in pure copper. Since the Cu $3d$ band in β'-CuZn arises mainly as an interaction between Cu atoms, one would expect this d band to be narrower than the corre-

TABLE IV. Widths and positions of the s, p, and d bands in β' − CuZn and Cu. The symmetry symbols in the table are those of the present work (Zn site as the origin for wave functions) whereas the symbols in the footnote belong to the particular reference.

	Width (Ry)				Position (Ry) relative to Γ_1		
	Burdick (Ref. 27) Cu	Present calc. CuZn	Arlinghaus (Ref. 17) CuZn	Amar, Johnson and Wang (Ref. 15) CuZn		Present calc. CuZn	Arlinghaus (Ref. 17) CuZn
Zn d band							
Γ'_{25}-Γ_{12}		0.031	0.034		Γ_{12}	-0.055	-0.031
R_{12}-R'_{25}		0.039	0.040		R'_{25}	-0.012	0.018
Cu d band							
Γ'_{25}-Γ_{12}		0.066	0.070	0.06	Γ_{12}	0.437	0.458
M_4-M_1		0.153	0.163	0.11	M_1	0.363	0.384
X'_5-X_1	0.249[a]	0.174	0.200	0.17[b]	X_1	0.326	0.327
T'_1-T_1		0.135	0.144	0.10			
R'_{12}-R_{15}		0.114	0.119	0.11	R_{15}	0.404	0.426
s band							
R_1-Γ_1		1.017	1.032	0.90[c]	Γ_1	0.	0.
p band							
M'_4-X'_4		1.178	1.18		X'_4	0.563	0.586

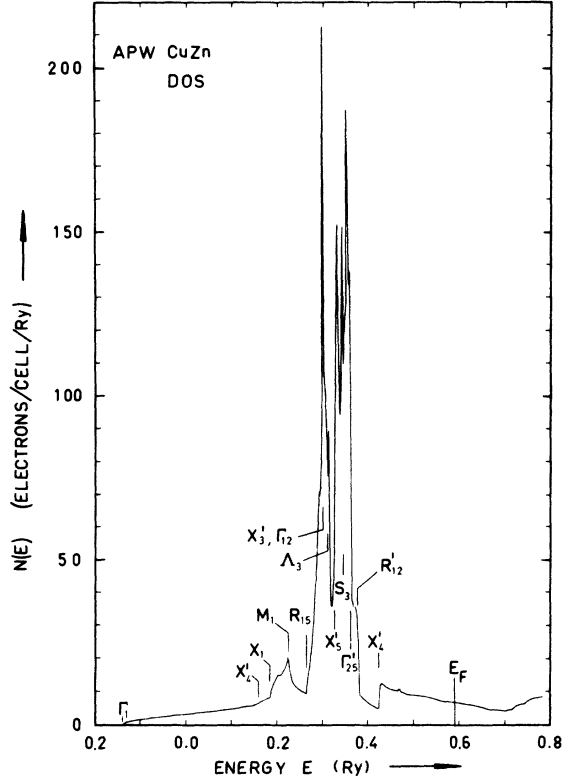[a]X_5-X_1.   [b]X_3-X_1.   [c]R_{15}-Γ_1.

FIG. 4. Density of states for β' -CuZn as calculated from the original 13 bands found at 84 points in $\frac{1}{48}$ of the Brillouin zone. A list of these 1092 eigenvalues is found in Table III. The main van Hove singularities are indicated on the figure in order to compare the density-of-states function with the energy bands in Fig. 3.

sponding band in copper. This is indeed what we find judged from the energy separations listed in Table IV or from the calculated densities of states for β'-CuZn (Fig. 4) and for Cu.[23,27]

A. Density-of-States Functions

The one-electron density of states is defined by an integral over the surface of energy E^0,

$$N(E^0)= \frac{2\Omega}{(2\pi)^3} \int \frac{dS_{E^0}}{|\vec{\nabla}_k E(\vec{k})|} , \qquad (1)$$

where Ω is the volume of the unit cell. In the case of the noble metals[25,29] a good procedure to calculate density-of-states functions from energy eigenvalues determined at a limited number of k points appeared to be a local Lagrange interpolation scheme combined with the method of Gilat and Raubenheimer.[30] We have adopted this procedure in the present work with 8436 interpolated k points in $\frac{1}{48}$ zone, and the result for the one-electron density of states for β'-CuZn is shown in Fig. 4. The Cu d band is clearly seen as the group of narrow peaks superimposed on the free-electron parabola $N(E)$

$\propto E^{1/2}$.

It follows from Eq. (1) that the Fermi level can be found as the energy satisfying

$$\int_{E_1}^{E_F} N(E)dE=n , \qquad (2)$$

where E_1 is some energy lying between the Zn d band and the bottom of the common s band, and n, the number of electrons per unit cell, is 13. The Fermi energy was found (i) by integrating the density of states Eq. (2), (ii) by the counting of the original APW eigenvalues, and (iii) by integrating constant-energy surfaces. The latter method is carried out by finding the surface having a volume of 1.5 times the volume of the Brillouin zone since there are three conduction electrons per unit cell. The results agree within 2 mRy giving $E_F = 0.590$ Ry on the APW scale. $N(E_F)$ is found to be 6.68 (electrons/cell)/Ry (Fig. 4) which compared to the value of 8.06 (electrons/cell)/Ry obtained from the electronic-heat-capacity measurements[6] suggests an average apparent mass enhancement of 0.19. This is not an unreasonably large value in view of the 0.12 found for copper.[31]

The joint-density-of-states function, which gives the density of transitions of energy $\hbar\omega$ from bands below the Fermi level to bands above the Fermi level, can be found from

$$J(\hbar\omega)= \frac{2\Omega}{(2\pi)^3} \sum_{i,f} \int \delta(E_f(\vec{k}) - E_i(\vec{k}) - \hbar\omega)d\vec{k} , \qquad (3)$$

where $E_i(\vec{k}) \leq E_F$ and $E_f(\vec{k}) \geq E_F$. This function consists of a sum of partial joint-density-of-states functions $J_{if}(\hbar\omega)$, each of which gives the density of vertical transitions of energy $\hbar\omega$ from that part of band i which is below E_F to that part of band f which is above E_F. The band indices of $J_{if}(\hbar\omega)$ run over states of increasing energy for a given $\vec{k}$.
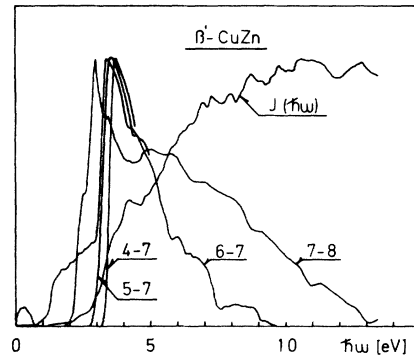
We have shown in Fig. 5 the calculated joint den-

FIG. 5. Joint density of states and four partial joint-density-of-states functions for β' -CuZn. All curves have been scaled to the same maximum value with the following scaling factors: (6-7), $\frac{1}{3330}$; (7-8), $\frac{1}{2710}$; (5-7), $\frac{1}{5040}$; (4-7), $\frac{1}{4590}$.

sity of states as well as some partial joint-density-of-states functions for β'-CuZn. The partial functions shown are important in comparison with experiment because they have appreciable values in the energy range near the fundamental absorption edge. Since the Fermi level crosses the doubly degenerate T_5 and the two nearly degenerate S_1 and S_3 bands, the joint density of states increases from zero energy. This can be seen from $J_{67}(\hbar\omega)$ in Fig. 5. Although spin-orbit splitting typically of the order of 0.1 eV will remove the degeneracy of the T_5 level, the density will still have nonzero values in the range below 1 eV. This means that one has to be cautious when estimating the optical mass by the usual Drude theory.

The partial joint-density-of-states function $J_{67}(\hbar\omega)$ has contributions from two types of transitions. Below 3 eV the important contribution comes from transitions between conduction states while the edge at 3 eV has its origin in transitions from the top of the Cu d band to the Fermi level, $\Delta'_2 \rightarrow \Delta_1$. The latter transition, however, is forbidden according to the optical selection rules. One might therefore argue that the peak at 3.4 eV should be reduced in a calculation of the dielectric constant although this would be a very crude way of considering the effect of the dipole matrix elements. Only transitions between conduction states contribute to $J_{78}(\hbar\omega)$. Thus, the edge at 1.9 eV comes from transitions from the Fermi level to a higher-lying band near $T_5(E_F) \rightarrow T_1$ while the edge at 2.6 eV has its origin in the analogous transitions near $\Sigma_4(E_F) \rightarrow \Sigma_1$. Both transitions are allowed according to the selection rules. The remaining functions $J_{47}(\hbar\omega)$ and $J_{57}(\hbar\omega)$ include transitions from the d band to the Fermi level.

The energy distribution of the joint density of states, defined by

$$D(E_i^0, \hbar\omega) \propto \sum_{i,f} \int \delta(E_f(\vec{k}) - E_i(\vec{k}) - \hbar\omega)$$
$$\times \delta(E_i^0 - E_i(\vec{k}))d\vec{k}, \qquad (4)$$

where $E_i(\vec{k}) \leq E_F$ and $E_f(\vec{k}) \geq E_F$, forms under the assumption of constant dipole matrix elements and $\vec{k}$ conservation the basis for the interpretation of photoemission experiments in the so-called direct model. If $\vec{k}$ conservation is not considered an important selection rule, one would interpret the photoemission experiments in terms of a product of density-of-states functions taken at the initial and the final energies,[32] i.e., $N(E_i^0)N(E_i^0 + \hbar\omega)$. This constitutes the nondirect model.

The applicability of a specific model depends on how well the electrons that are excited can be regarded as being itinerant or localized.[33,34] In the noble metals even the d states appear to be nonlocalized, and for these metals the direct model
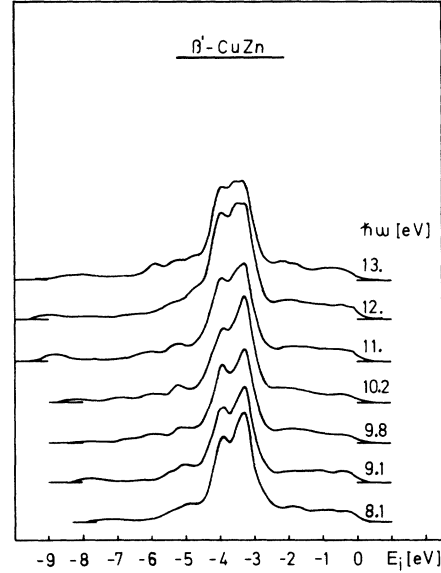

FIG. 6. Velocity-modulated energy distribution of the joint density of states for β'-CuZn as a function of the initial energy calculated for several photon energies. All curves have been folded with a Lorentzian of full half-width 0.3 eV.

gives satisfactory results,[25,35,36] although one cannot completely rule out nondirect transitions. Since the Cu d band in β'-brass has a width around 70% of the width of the d band in copper, one might expect the direct model also to apply in the alloy case. However, in the presence of flat d bands the two models give similar results, and one cannot distinguish between the two models in the present case.

The energy distribution of the joint density of states for several photon energies is shown in Fig. 6 with the following modification: The integrand in Eq. (5) has been multiplied by the velocity of the final state since it is difficult for an electron with zero velocity to contribute to the photoemission spectrum—though elastic scattering to a state with nonzero velocity is a possibility. The main features of the calculated curves are the two peaks at −3.3 and −3.9 eV which have their origin in the Cu d band. These peaks remain stationary throughout the entire photon energy range, and the first of them splits into two at higher photon energies. In addition to this a peak emerges at −5.0 eV for $\hbar\omega \geq 8.1$ eV and is found at −5.3 eV for $\hbar\omega = 10.2$ eV.

B. Comparison with Optical Measurements

If one can assume the dipole matrix elements to be constant, then the interband contribution to the imaginary part of the dielectric constant, $\epsilon_2^i(\omega)$, will be proportional to the joint density of states divided by ω^2. It is therefore convenient to com-
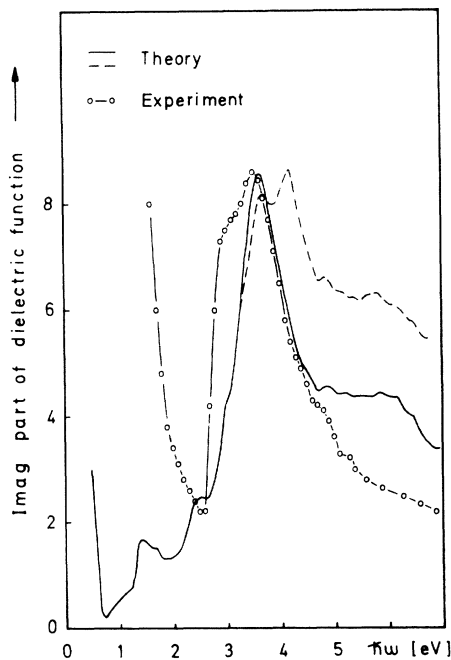
FIG. 7. Comparison between $J(\hbar\omega)/\omega^2$ and the experimentally (Ref. 3) recorded imaginary part, $\epsilon_2(\omega)$, of the dielectric function. The curve indicated by a broken line represents the total $J(\hbar\omega)/\omega^2$, whereas transitions from the three lowest bands have been omitted in the curve drawn with full line.

pare the experimental[3,4] $\epsilon_2(\omega)$ with the calculated $J(\hbar\omega)/\omega^2$ as is done in Fig. 7. In this comparison one should note that the calculated curves do not include a low-energy contribution of the Drude form from the conduction electrons and that the sudden rise in the calculated $\epsilon_2^i(\omega)$ below 1 eV is a pure interband effect.

Because of the complicated shape of the joint-density-of-states function below 3 eV and the unknown matrix elements, it is not possible to define unambiguously a theoretical absorption edge. One can say only that the calculated $\epsilon_2^i(\omega)$ rises sharply between 2 and 3 eV. Furthermore, the onset of transitions between conduction states $[J_{78}(\hbar\omega)]$ and the onset of transitions from the top of the Cu d band $[J_{67}(\hbar\omega), J_{57}(\hbar\omega)]$ are so close in spectral position that one should ascribe the fundamental absorption edge to both types of transitions.

The calculated main peak results from transitions from the Cu d band. It is split into two peaks and has contributions from four partial functions. The two functions, $J_{47}(\hbar\omega)$ and $J_{57}(\hbar\omega)$, contributing to the first of these peaks were shown in Fig. 5. The edge in one, $J_{37}(\hbar\omega)$, of the two partial functions giving the second peak results from forbidden transitions ($\Delta_2 \rightarrow \Delta_1$) so that the inclusion of matrix elements might reduce this second peak. If one excludes transitions from the three lowest bands, the

second peak vanishes completely and the shape of $\epsilon_2^i(\omega)$ is well predicted by the calculation. Similar conclusions were reached in the case of silver[37] and gold.[25]

Since the d band is responsible for the calculated main peak and since this peak is displaced above the corresponding experimental peak, we conclude that the top of the present Cu d band lies too far below the Fermi level. This is in accord with the photoemission calculation. It may be seen in Fig. 7 that, with the above empirical inclusion of matrix elements, the apparent error in the position of the top of our theoretical d band is less than 0.2 eV when compared to the experiments of Ref. 3. When compared to the measurements of Ref. 4, the error is 0.4 eV.

C. Comparison with Photoemission Experiments

A theoretical EDC may be calculated by folding the energy distribution of the joint density of states $D(E_i^0, \hbar\omega)$ or the product of density-of-states functions with a Lorentzian of half-width Γ, and multiply the function obtained by the appropriate escape and threshold functions. These escape and threshold functions were taken to be similar to those used by Berglund and Spicer,[32] and they include the optical absorption coefficient $\alpha(\omega)$,[4] the work function $e\phi$ which for β'-CuZn is 4.4 eV,[38] and an energy-dependent mean free path $L(E)$ adjusted to be 25 Å at 8 eV. The latter is the experimental value of $L(E)$ for copper[39] which we apply in the present
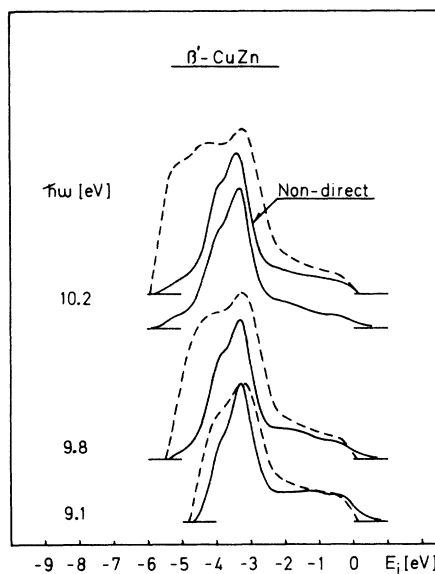

FIG. 8. Comparison between experiment (Ref. 5) (dashed lines) and EDC's calculated from the direct model (solid lines) for several photon energies. At $\hbar\omega = 10.2$ eV the result of the nondirect model is also shown. All the calculated curves have been folded by a Lorentzian of full half-width 0.5 eV.

case although we realize that the mean free paths
in the alloy may differ considerably from those of
Cu. Calculations show, however, that an adjust-
ment of $L(E)$ to 50 Å at 8 eV or even 75 Å does not
influence the spectra significantly.

The experimental EDC's[5] display two peaks at
-3.3 and -4.3 eV, respectively, but very little
additional structure, although a bump is seen at
-5.3 eV. We have compared the experimental and
the calculated EDC's for some photon energies in
Fig. 8. In this comparison one should note that we
have neglected both the variation of matrix ele-
ments and the effect of inelastically scattered elec-
trons which tend to fill up the low-energy side of
the spectrum. The direct and the nondirect models
are found to give very similar results except for
$\hbar\omega = 10.2$ eV. The difference at 10.2 eV is due to
the velocity modulation in the direct model, men-
tioned at the end of Sec. III A, since the final states
giving the peak at -3.9 eV are close to the Γ_{15} lev-
el where $v_f \simeq 0$. The experiments, however, do
not seem to support this velocity modulation.

The peak at -3.3 eV is seen to be predicted
rather accurately by the calculation. It is found to
have its origin in transitions from the minimum in
the S_3 level midway between R and X (Fig. 3) and is
therefore not directly related to the top of the d
band. However, judged from the onset of the d
band structure in the calculated EDC, the top of
the present Cu d band may be found to be positioned
0.2 eV too far below the Fermi level in agreement
with the $\epsilon_2^i(\omega)$ calculation. The bump at -5.3 eV
in the experimental curves for $\hbar\omega \geq 9.8$ eV may be
related to the structure which for $\hbar\omega = 10.2$ eV oc-
curs at -5.3 eV in the calculated EDC's (see also
Fig. 6).

For higher photon energies both models, at least
in the region of flat d bands, will reflect the den-
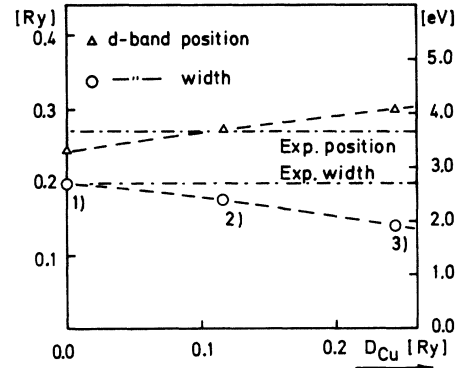
FIG. 10. Calculated Cu d-band parameters, width and
position, as functions of the discontinuity at the copper
muffin-tin sphere. The width is defined as the energy
separation X_5^i-X_1, and the position is taken as the posi-
tion of the center of gravity relative to the Fermi level.
The data are from (1) Ref. 16, (2) the present calcula-
tion, and (3) Ref. 18. The experimental width and posi-
tion are deduced from the EDC (Ref. 5) at $\hbar\omega = 21.2$ eV
(Fig. 9).

sity of initial states. Furthermore, the inelastical-
ly scattered electrons do not interfere with the d-
band structure in the EDC since they are removed
to large negative values of the initial energy. One
can therefore get a qualitative measure of the ac-
curacy of the calculated d-band parameters, width
and position, by comparing a density-of-states
function with an experimental EDC taken at high
photon energy. This is done in Fig. 9 for $\hbar\omega = 21.2$
eV, where one should note that the experimental
EDC still has some background of inelastically
scattered electrons.

D. Cu 3d-band Parameters

In a comparison with experiments it is conve-
nient to define the position of the entire d band as
the position of the center of gravity (3.7 eV below
E_F in the present case) of the individual d levels as
estimated from the density of states. Using this
definition our Cu d band has the correct position—
judged from Fig. 9—whereas the apparent displace-
ment of the d-band top by 0.2-0.4 eV indicates that
the calculated d band is somewhat too narrow:
~ 0.4 eV also judged from Fig. 9. The Cu d band
in the first calculation by Arlinghaus[16,17] compared
nicely in width to the EDC at $\hbar\omega = 21.2$ eV, but its
position had to be shifted downwards by 0.4 eV.[5]
The most recent calculation[19] gave a d band too
narrow and positioned a little too far below the
Fermi level (Table I).

The above discussion is summarized in Fig. 10
by plotting the d-band parameters as functions of
the discontinuities at the muffin-tin spheres for the
various potentials. From this plot it seems clear
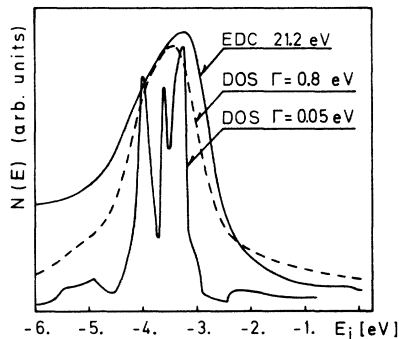that one cannot determine a discontinuity giving

FIG. 9. Comparison between an EDC (Ref. 5) at $\hbar\omega$
$= 21.2$ eV and two broadened density-of-states functions
obtained by folding the function in Fig. 4 with Lorentzian
of full half-widths 0.05 and 0.8 eV. The experimental
trace has a background contribution increasing towards
the left.

simultaneously correct width and position of the Cu $3d$ band.

There is one further problem related to the interpretation of the d-electron structure in the photoemission data which should be mentioned. If the escape depth becomes comparable to the lattice spacing which may occur for β'-CuZn at $\hbar\omega = 21.2$ eV, one would expect to see a surface emission rather than a bulk effect. In many materials[40,41] the d overlap would be reduced towards the surface because of the expansion of the lattice and the reduction in the number of nearest neighbors. In β'-brass, however, dezincification is likely to occur and may increase the d overlap towards the surface leading in the EDC to a d-like structure somewhat broader than the corresponding structure from the bulk d electrons. Thus, the effect of surface emission may reduce the gap between the experimental "d-band width" as determined from EDC's at high photon energies and the width calculated from the energy bands.

FIG. 12. Second-zone sheet of the Fermi surface as sketched from the actually calculated cross sections. Some extremal cross sections have been indicated.

IV. FERMI SURFACE

The free-electron Fermi sphere for β'-CuZn has a radius $k_F = 1.420\,\pi/a$ which is slightly larger than the ΓM distance (Fig. 1). Consequently, it leaves in the first zone a hole surface centered at R, and this hole has the shape of an octahedron when regarded in the repeated zone scheme (Fig. 11). In the second zone the Fermi sphere leaves six electron lenses, one at each side of the first-zone cube. Regarded in the repeated zone scheme, these segments have the form of convex lenses touching each other near M. The lenses are in the actual calculation perturbed by necks lying perpendicular to the $\langle 110 \rangle$ direction. However, they can still be recognized on the sketch (Fig. 12) of the second-zone electron sheet.

One can map out a constant-energy surface by the APW method programed for k search, and this was done at 570 points in $\frac{1}{48}$ zone for three surfaces of energy near the Fermi level. These raw data were then used in conjunction with a second-order
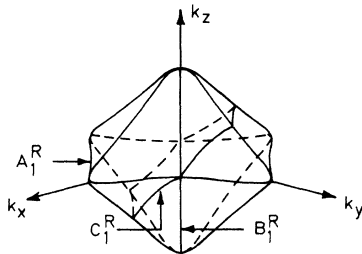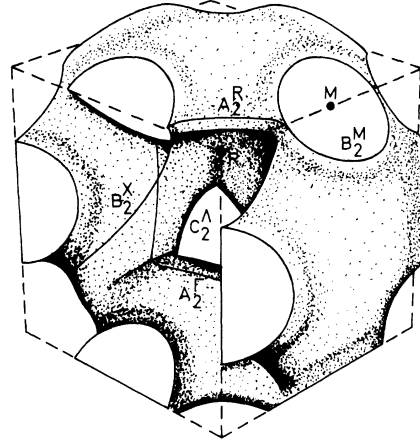
interpolation procedure to obtain extremal cross sections and their angular dependence, cyclotron masses, and Fermi velocities.

Many extremal orbits of β'-brass can be found by straightforward inspection. This is the case for the central orbits lying in symmetry planes [Figs. 13(a), 13(b), and 13(d)]. In addition to these orbits, β'-CuZn has noncentral extremal cross sections [Fig. 13(c)] which are determined from the requirement that the derivative of the cross-sectional area with respect to the k component in the direction of the magnetic field should vanish.

We use the conventional labeling[9] according to the normal of the orbit planes. Thus, A stands for a $\langle 100 \rangle$ direction, B for a $\langle 110 \rangle$ direction, and C for a $\langle 111 \rangle$ direction. A subscript designates the zone number, and a superscript gives the label of the symmetry point or line of the orbit. Later, in the calculation of the dHvA branches, we will refer to these branches by the label of the particular symmetry point or line with the zone number as the subscript.

The important central extremal cross sections are from the first-zone hole octahedron: A_1^R, B_1^R, and C_1^R; and from the second-zone electron lenses: a hole orbit A_2^Γ, an electron orbit around the lens B_2^X, a hole orbit A_2^R, and a neck orbit B_2^M. The noncentral orbits are: a dog's-bone hole orbit B_2^Σ, the triangular hole orbit C_2^Λ, a hole orbit B_2^Λ, an electron orbit A_2^Z, and the double hole orbit B_2^S all from the second zone.

Because of the overlap of the $k_z = 0$ and π/a cross sections of the Fermi surface found in previous calculations,[13-18] one would expect open orbitals along the $\langle 100 \rangle$ direction when $\vec{B}$ is close to the $\langle 110 \rangle$ direction. These are called type-I open orbits by Sellmyer $et\ al.$,[8] and they would not exist if $M\Sigma' > RS' > RQ$ (Fig. 14). This criterion is fulfilled

FIG. 11. First-zone hole sheet, the octahedron, of the Fermi surface as sketched from the actually calculated cross sections.
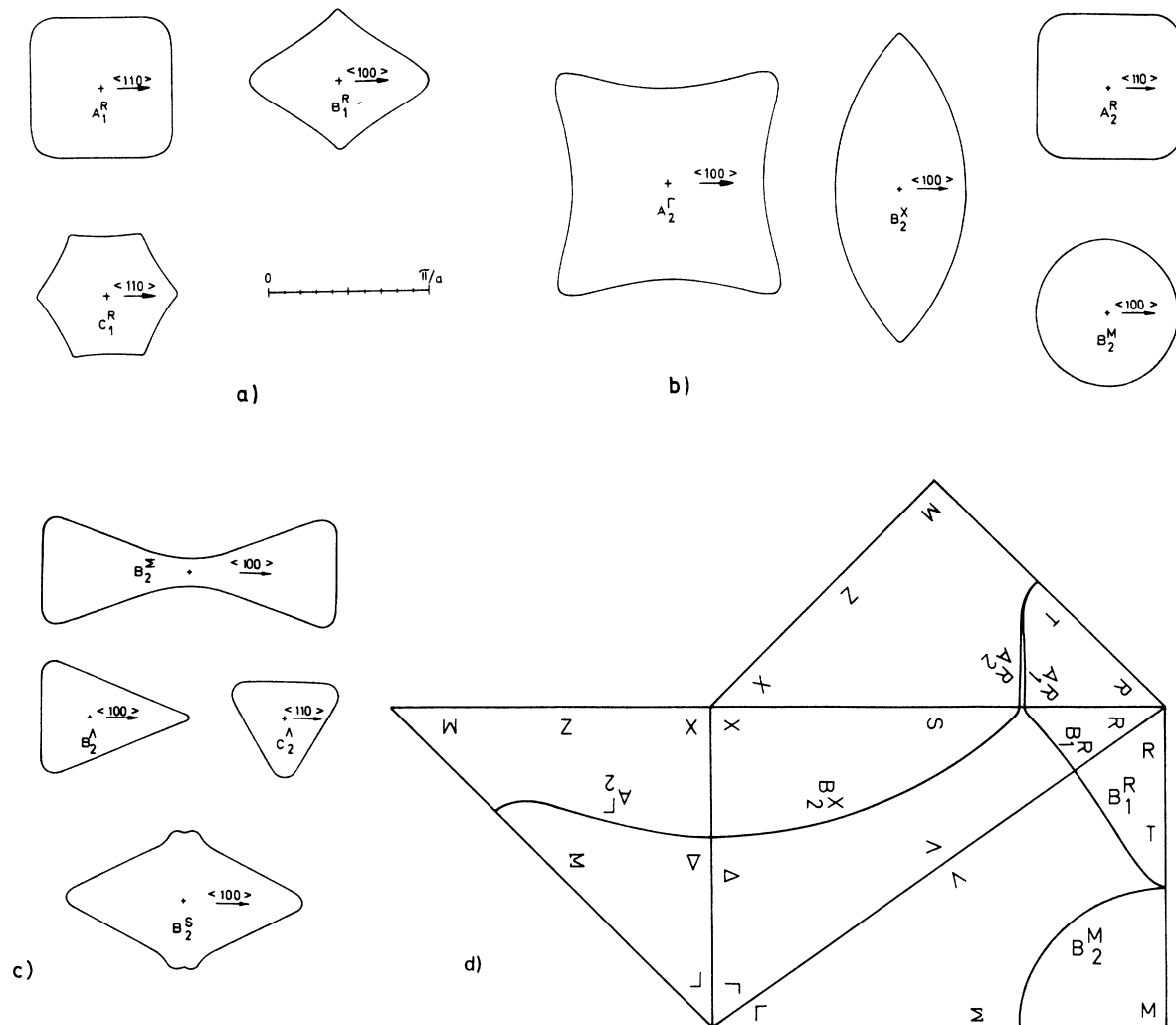
FIG. 13. First- and second-zone extremal cross sections of the Fermi surface. (a) First-zone central orbits, (b) second-zone central orbits, (c) noncentral orbits, and (d) first- and second-zone central orbits drawn on the surfaces of the irreducible zone.

in the present calculation (Table V), and in contrast to the previous calculations we therefore find a *closed* orbit B_2^Λ when $\vec{B}$ is parallel to the $\langle 110 \rangle$ direction. The general appearance of the present Fermi-surface model, however, is in good agreement with other calculations.[13-18] The shape of the two sheets sketched in Figs. 11 and 12 is in accordance with the latest work by Arlinghaus,[18] but is somewhat smoother than the shape of the surfaces constructed by Jan *et al.*[9] from cross sections calculated by Arlinghaus.[16,17] The cross-sectional areas of the present Fermi surface are also in good agreement with those determined by Arlinghaus[18] in symmetry directions (Table VI). In addition to his results we find four extra extremal cross sections of importance in the comparison with dHvA measurements.

A. Interpretation of de Haas-van Alphen Experiments

Since the de Haas–van Alphen measurements result in detailed knowledge of the dHvA frequencies as a function of the direction of the magnetic field, we have calculated the angular variation of extremal cross sections of the Fermi surface of β'-CuZn. The results are presented in Fig. 15 for fields in the {100} and the {110} planes together with the experimental results by Karlsson[10] and those by Jan and Perrot.[12]

The Λ_2 branch arises from orbits of the triangular hole centered on Λ at a distance around $1.14\pi/a$ from Γ. The center moves slightly as the plane of the orbit rotates. The branch starts in the {110} plane at 23° from $\langle 100 \rangle$ and exists all the way to $\langle 110 \rangle$, then it crosses the symmetry direction and disappears at 0.5° from $\langle 110 \rangle$. In the {100} plane,

TABLE V. Fermi-surface dimensions in units of $2\pi/a$ relevant for the existence of an open orbit along $\langle 100 \rangle$ with $\vec{B} \parallel \langle 110 \rangle$. Compare also with Fig. 14.

	Johnson and Amar (Ref. 15)	Arlinghaus (Ref. 17)	Present calc.
MT'	0.29	0.23	0.213
RQ^a	0.15	0.19	0.203
RS'	0.28	0.28	0.225
$M\Sigma'$	0.20	0.21	0.231

$^a RQ = RT'/\sqrt{2}$.

the Λ_2 branch can only be observed up to 1.5° from the $\langle 110 \rangle$ direction. The excellent agreement of the Λ_2 branch with both the angular variation in the $\{110\}$ plane and the crossing at $\langle 110 \rangle$, observed by Jan and Perrot,[12] shows that F_1 is in fact associated with the triangular hole as stated by Taylor.[19]

The existence of the closed B_2^Λ orbit and the crossing of the Λ_2 branch at $\langle 110 \rangle$, supported by the measurements, are particularly satisfying since these two features are a direct consequence of the nonexistence in the present model of the open orbits along $\langle 100 \rangle$ for $\vec{B} \parallel \langle 110 \rangle$. On this important point the present Fermi surface is therefore in agreement with both the dHvA experiments[12] and the magnetoresistance result.[8]

The R_1 branch originates in orbits of the octahedron. It can be observed for all angles in the two planes $\{100\}$ and $\{110\}$. At 4° from $\langle 110 \rangle$ in the $\{110\}$ plane, it has risen 1% above its value at $\langle 110 \rangle$. Although it does not rise as much as F_8 in

the $\{110\}$ plane, the behavior in the $\{100\}$ plane strongly indicates that we may assign the R_1 branch to both of the two newly discovered frequencies F_8 and F_5. F_5 and F_8 therefore seem to be part of the same branch. This was also considered as a possibility by Jan and Perrot.[12]

The M_2 branch comes from neck orbits and may be assigned to the experimentally observed F_2. The R_2 branch comes from the second-zone hole and may be assigned to F_3 although the angular variation is not in complete agreement with experimental data. The X_2 branch has its origin in orbits of the lens and extends beyond the $\langle 111 \rangle$ direction in the $\{110\}$ plane. It has not been observed experimentally.

Since the preliminary account of this work,[20] we have discovered three new noncentral extremal orbits: the dog's-bone B_2^C, the double hole B_2^S, and an electron orbit A_2^Z. The Σ_2 branch containing the B_2^C orbit has its origin in orbits between the two lenses (Fig. 16) and exists in a range of some 30° in the $\{100\}$ plane. In the $\{110\}$ plane it can only be observed up to 1.5° from the $\langle 110 \rangle$ direction. At $\langle 110 \rangle$ the minimum in the cross-sectional area leading to B_2^C is very sharp, indicating that the dHvA amplitude of the Σ_2 branch should be rather weak. In view of the angular dependence in the $\{100\}$ plane, we have assigned F_4 to the Σ_2 branch.

The S_2 branch of the double hole B_2^S comes from orbits running between four necks and exists only in a limited range of angles near the $\langle 110 \rangle$ direction (Fig. 16). We have associated this branch with the few unlabeled experimental points below F_2.

TABLE VI. Calculated and experimental extremal cross sections of the Fermi surface of β'-brass in units of $(2\pi/a)^2$.

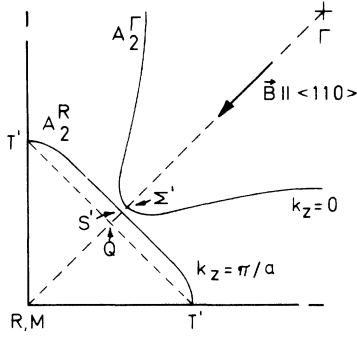|	Arlinghaus (Ref. 17)	Arlinghaus (Ref. 18)	Present calc.	Expt. (Ref. 11) Springford and Templeton	Expt. (Ref. 9) Jan, Pearson and Saito	Expt. (Ref. 12) Jan and Perrot
A_1^R	0.20	0.19	0.187			
A_2^R	0.24	0.21	0.195	0.1945	0.19	0.1946
A_2^Γ		0.41	0.407			
A_2^Z			0.135			
B_1^R	0.18	0.13	0.128	0.1333		0.1330
B_2^M	0.12	0.14	0.159	0.1696	0.17	0.1691
B_2^X		0.27	0.270			
B_2^Λ			0.091	0.0933		0.0940
B_2^S			0.170			0.1643
B_2^C			0.191			~0.20
C_1^R		0.12	0.121			
C_2^X		0.31	0.318			
C_2^Λ		0.07	0.066	0.0666	0.067	0.0666

FIG. 14. Fermi-surface cross sections in the two planes $k_z = 0$ and $k_z = \pi/a$ sketched from the calculated orbits showing the nonexistence in the present model of the type I (Ref. 8) open orbits.

FIG. 16. Intersection of the second-zone Fermi surface by a $\{110\}$ plane showing two central extremal orbits B_2^M and B_2^X. The broken lines indicate the intersection of the $\{110\}$ plane by the planes of the noncentral extremal orbits B_2^Σ, B_2^S, and B_2^Λ.

The two Z_2 branches containing A_2^Z have their origin in electron orbits on the lens. The extremum of the upper branch vanishes at $6°$ from $\langle 100 \rangle$ in the $\{100\}$ plane, but orbits exist to about $30°$ from $\langle 100 \rangle$. These orbits may become extremal beyond $6°$ and thereby account for F_{10}, but we have not been able to prove this, mainly because the center of the orbits moves very fast along Z as the plane of the orbits rotates. The lower Z_2 branch disappears at $13°$ from $\langle 100 \rangle$. We may associate the Z_2 branches with the two unlabeled points in the $\{100\}$ plane.
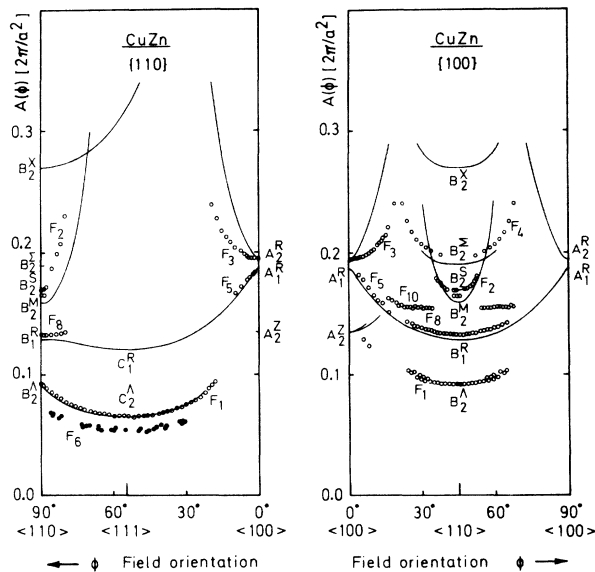
We have now accounted for all the experimental

dHvA branches except for F_6 seen by Karlsson[10] and F_{10}. In Ref. 20 a tentative explanation of F_6 was given in terms of the difference between the R_1 and Λ_2 branches. This explanation, however, is in contradiction[42] with the experimental points of F_6, F_1, and F_8 near $\langle 110 \rangle$. At the moment there is therefore no clear explanation for F_6 and F_{10}.

We have in Table VI listed the extremal areas in symmetry directions from three calculations and compared them to the experimental values. We find excellent agreement between the present calculation and the experimental results, and this comparison together with the more detailed comparison with the dHvA branches shows clearly that the present band structure of β'-CuZn yields a Fermi surface which explains the main portion of the Fermi-surface measurements.

B. Effective Masses

The cyclotron mass at a given extremal cross section of the Fermi surface can be found from the relation

$$ \frac{m_c}{m_0} = \frac{\hbar^2}{2\pi m_0} \frac{\partial A}{\partial E}\bigg|_{E_F} , \tag{5} $$

where m_0 is the free-electron mass. We have examined the variation of the cross-sectional areas with energy by calculating two constant-energy surfaces of energy $E_F - 10$ mRy and $E_F + 10$ mRy. Thus, we have been able to estimate the cyclotron masses of β'-CuZn not only along symmetry directions (Table VII), but also as a function of the direction of the magnetic field (Fig. 17).

The calculated cyclotron masses include the effect of the crystal potential and give a measure of the deviations of the actual band structure from the free-electron bands at the Fermi level. Because of the additional effect of the electron-electron and the electron-phonon interactions, the band masses may deviate considerably from the measured values (Table VII). The ratio between the experimentally determined masses and the calculated band

FIG. 15. Calculated extremal areas in the $\{110\}$ and the $\{100\}$ planes for β' -CuZn (solid lines). Also shown are the dHvA frequencies measured by Jan and Perrot (Ref. 12)—open circles—and by Karlsson (Ref. 10)—closed circles.
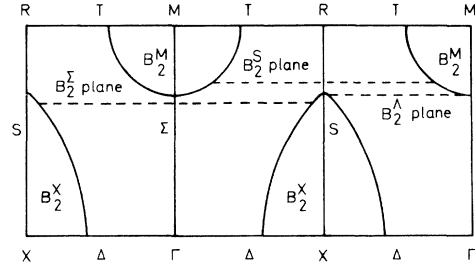
TABLE VII. Calculated cyclotron masses of β' -CuZn along symmetry directions compared to the experimentally obtained masses.

	Present calc.	Jan and Perrot (Ref. 12)	Ratio
	m_{theor}/m_0	m_{expt}/m_0	$m_{\text{expt}}/m_{\text{theor}}$
A_1^R	0.61		
A_2^R	0.61	0.72 ± 0.01	1.18
B_1^R	0.39	0.55 ± 0.01	1.41
B_2^M	0.67	0.88 ± 0.08	1.31
B_2^X	0.55		
B_2^Λ	0.46	0.60 ± 0.03	1.30
C_1^R	0.37		
C_2^X	0.65		
C_2^Λ	0.30	0.37 ± 0.01	1.23
		0.42^a	
		0.56^b	

[a]From Ref. 9.   [b]From Ref. 11.

masses leads to an anisotropic apparent mass enhancement varying between 0.18 and 0.41. For pure copper[31] the calculated electron-phonon renormalization was found to vary between 0.1 and 0.2 in partial agreement with the above values for β'-brass.

V. SUMMARY AND CONCLUSIONS

The electronic structure of the ordered alloy β'-CuZn has been calculated from a nonrelativistic one-electron potential of the muffin-tin form using full Slater exchange. The energy bands are found to be in qualitative agreement with other calculations which apply the same type of potential but with different discontinuities at the muffin-tin spheres.

The fundamental optical absorption edge as determined from the calculated imaginary part of the dielectric function, $\epsilon_2^i(\omega)$, lies in the range between 2 and 3 eV below the Fermi level in agreement with the optical measurements. It is also found, assuming constant dipole matrix elements, that both transitions between conduction states and transitions from the Cu d band determine the absorption edge.

The EDC's calculated in the direct as well as the nondirect model agree well with the photoemission experiments showing that the Cu d band in the present work has the correct position. Both the optical and the photoemission experiments, however, indicate that the present Cu d band is 25% too narrow. In a comparison with other potentials it is found impossible to obtain a Cu d band of both correct position and correct width by adjusting the discontinuities at the muffin-tin spheres.

The presented Fermi-surface model gives extremal cross sections which, in symmetry directions, are in good agreement with other calculations. In addition to these calculations we find four new extremal cross sections of importance in the interpretation of the dHvA results. The open orbit along the $\langle 100 \rangle$ direction predicted by all the previous calculations has now developed into a closed orbit B_2^Λ. This is in agreement with the magnetoresistance result as well as the dHvA measurements. The calculated angular variation of the extremal cross sections is found to be in excellent agreement with the dHvA results. A connection between orbits on the Fermi surface and the main portion of the experimental dHvA branches has been established. The effective cyclotron masses have been determined as functions of the direction of the magnetic field. A comparison between the experimental cyclotron masses and those derived from the present band structure in symmetry directions shows an apparent mass enhancement varying between 0.18 and 0.41. The ratio between the experimentally obtained and the calculated density of states at the Fermi level indicates a Fermi-surface average of the apparent mass enhancement of 0.19.
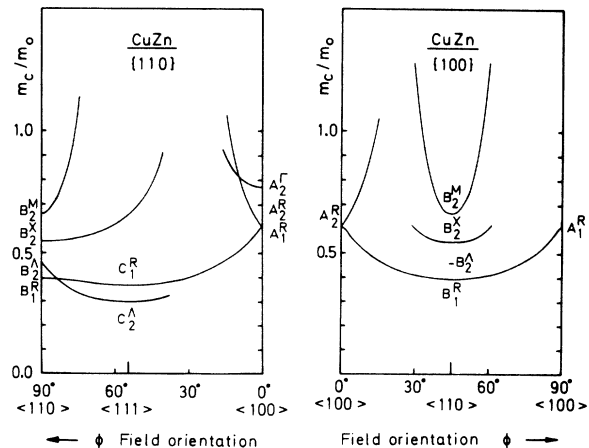
FIG. 17. Calculated cyclotron masses in the {110} and the {100} planes as functions of the direction ϕ of the magnetic field.

[1]W. Hume-Rothery, J. Inst. Met. **35**, 295 (1926).

[2]L. Muldawer, Phys. Rev. **127**, 1551 (1962).

[3]L. Muldawer and H. J. Goldman, in *Optical Properties and Electronic Structure of Metals and Alloys*, edited by F. Abeles (North-Holland, Amsterdam, 1966).

[4]J.-P. Jan and S. S. Vishnubhatla, Can. J. Phys. **45**, 2505 (1967).

[5]P. O. Nilsson and I. Lindau, J. Phys. F **1**, 854 (1971).

[6]B. W. Veal and J. A. Rayne, Phys. Rev. **128**, 551 (1962).

[7]V. Frank, K. Dan. Vidensk. Selsk. Mat.-Fys. Medd. 30, (4) (1955).

[8]D. J. Sellmyer, J. Ahn, and J.-P. Jan, Phys. Rev. **161**, 618 (1967).

[9]J.-P. Jan, W. B. Pearson, and Y. Saito, Proc. R. Soc. A **A297**, 275 (1967).

[10]A. Karlsson, J. Low Temp. Phys. **1**, 59 (1969).

[11]M. Springford and I. M. Templeton, J. Low Temp. Phys. **5**, 113 (1971).

[12]J.-P. Jan and C. M. Perrot, J. Low Temp. Phys. **8**, 195 (1972).

[13]K. H. Johnson and H. Amar, Phys. Rev. **139**, A760 (1965).

[14]K. H. Johnson and H. Amar, in Ref. 3.

[15]H. Amar, K. H. Johnson, and P. K. Wang, Phys. Rev. **148**, 672 (1966).

[16]F. J. Arlinghaus, Quarterly Progress Report, Solid State and Molecular Theory Group, MIT, No. 56 (1965) (unpublished).

[17]F. J. Arlinghaus, Phys. Rev. **157**, 491 (1967).

[18]F. J. Arlinghaus, Phys. Rev. **186**, 609 (1969).

[19]R. Taylor, Proc. R. Soc. A **321**, 495 (1969).

[20]H. L. Skriver, Solid State Commun. **11**, 1355 (1972).

[21]F. Herman and S. Skillman, *Atomic Structure Calculations* (Prentice Hall, Englewood Cliffs, N. J., 1963).

[22]J. C. Slater, in *Computational Methods in Band Theory*, edited by P. M. Marcus, J. F. Janak, and A. R. Williams (Plenum, New York, 1971).

[23]N. E. Christensen (unpublished).

[24]N. E. Christensen, Phys. Status Solidi **31**, 635 (1969).

[25]N. E. Christensen and B. O. Seraphin, Phys. Rev. B **4**, 3321 (1971).

[26]L. P. Bouchaert, R. Smoluchowski, and E. Wigner, Phys. Rev. **50**, 58 (1936).

[27]G. A. Burdick, Phys. Rev. **129**, 138 (1963).

[28]L. F. Mattheiss, Phys. Rev. **134**, A970 (1964).

[29]N. E. Christensen, thesis (Phys. Lab. I, Technical University of Denmark, 1970), Report No. 75 (unpublished).

[30]G. Gilat and L. J. Raubenheimer, Phys. Rev. **144**, 390 (1966).

[31]D. Nowak, Phys. Rev. B 6, 3691 (1972).

[32]C. N. Berglund and W. E. Spicer, Phys. Rev. **136**, A1044 (1964).

[33]W. E. Spicer, Phys. Rev. 154, 385 (1967).

[34]S. Doniach, Phys. Rev. B 2, 3898 (1970).

[35]N. E. Christensen, Phys. Lett. A **35**, 206 (1971).

[36]N. E. Christensen, Phys. Status Solidi **52**, 241 (1972).

[37]N. E. Christensen, Phys. Status Solidi **54**, 551 (1972).

[38]P. O. Nilsson (private communication).

[39]H. Kanter, Phys. Rev. B 1, 522 (1970).

[40]R. Haydock, V. Heine, and M. J. Kelly, J. Phys. C **5**, 2845 (1972).

[41]R. Haydock, V. Heine, M. J. Kelly, and J. B. Pendry Phys. Rev. Lett. **29**, 868 (1972).

[42]J.-P. Jan (private communication).